Journal of ELECTRONIC MATERIALS, Vol. 47, No. 3, 2018
https://doi.org/10.1007/s11664-017-5997-4

A Rapid Deposition of Fluorine Doped Zinc Oxide Using the Atmospheric Pressure Chemical Vapour Deposition Method

NAVID NAJAFI[1] and S.M. ROZATI[1,2]

1.—Physics Department, University of Guilan, Rasht, Iran. 2.—e-mail: smrozati@guilan.ac.ir

Fluorine-doped zinc oxide (FZO) (ZnO:F) thin films were manufactured by atmospheric pressure chemical vapor deposition (APCVD) on glass substrates using zinc acetate dihydrate [$C_4H_6O_4Zn{\cdot}2H_2O$, ZnAc] and ammonium fluoride (NH_4F) as the source of fluorine with deposition duration of only 120 s for each sample. The effects of different amounts of fluorine as the dopant on the structural, electrical and optical properties of FZO thin films were investigated. The results show a polycrystalline structure at higher temperatures compared to amorphous structure at lower temperatures. The x-ray diffraction patterns of the polycrystalline films were identified as a hexagonal wurtzite structure of zinc oxide (ZnO) with the (002) preferred orientation. Also, the sheet resistance decreased from 17.8 MΩ/□ to 28.9 KΩ/□ for temperatures 325°C to 450°C, respectively. In order to further decrease the sheet resistance of the undoped ZnO thin films, fluorine was added using NH_4F as the precursor, and again a drastic change in sheet resistance of only 17.7 Ω/□ was obtained. Based on the field emission scanning electron microscopy images, the fluorine concentration in CVD source is an important factor affecting the grain size and modifies electrical parameters. Ultraviolet–visible measurements revealed reduction of transparency of the layers with increasing fluorine as the dopant.

Key words: Fluorine doped zinc oxide, chemical vapor deposition (CVD), thickness measurements, electrical resistivity, optical bandgap

INTRODUCTION

Zinc oxide (ZnO) is a wide band gap (3.37 eV) semiconductor with a large (60 meV) exciton binding energy. Piezoelectricity and high room temperature electron mobility in ZnO cause lasing action based on exciton recombination above room temperatures. ZnO has attracted lots of interest because of its effect on fundamental studies and its diverse applications in ultraviolet and blue light emitting diodes, laser diodes, ferroelectric, piezoelectric, gas sensors, field effective transistors, and acoustic wave devices.[1–4] ZnO with a wurtzite structure, which is in fact a hexagonal crystal structure (lattice parameters: $a = b = 0.32427$ nm, $c = 0.51948$ nm), fits into the space group $P6_3mc$, and is identified by two interconnecting sublattices of O^{2-} and Zn^{2+}, in a way that Zn ions are surrounded by O ions, and vice versa.[5]

Fluorine doped zinc oxide (FZO) has been synthesized by various techniques such as sputtering[6,7] using reactive a radio frequency magnetron for creating the plasma in a vacuum condition from a pure ZnO and CF_2 gas, ZnF_2 ceramic targets and so on, but controling the quality of the thin films is usually difficult and F variations are limited. Other techniques are sol–gel with repeated dip coating[8] using zinc acetate and NH_4F as the source of zinc and fluorine and constant substrate removing and dipping speed of 3.3 cm/min into and from the solution, spray pyrolysis[9–11] with some variations such as using ultrasonic waves or an atomizer to produce very fine and uniform precursor droplets before reaching the substrate and depositing different fluorine concentrations, pulsed laser deposition

(Received December 20, 2016; accepted December 1, 2017; published online December 13, 2017)

(PLD)[12] by using a sintered target of ZnO, which contain ZnF_2 as the source fluorine in vacuum condition, vacuum arc plasma evaporation,[13] with high deposition rate resulting in thin films with uniform resistivity and thickness, and chemical vapor deposition (CVD)[14–17] which in turn consists of many variations and setups such as low pressure CVD (LPCVD), aerosol assisted CVD (AACVD), metal organic CVD (MOCVD), atmospheric pressure CVD (APCVD) and many more, each with their own advantages and drawbacks.

CVD of films and coatings results from chemical reactions of reactants in gaseous phase on or in close vicinity of an already heated substrate surface. The atomistic deposition process (APCVD) can provide very pure materials with a good structural control at nanometer or atomic scale level. It can also produce single layer, nanostructured, composite, multilayer, and functionally graded coatings with good controlled dimensions and unique structures at a low temperature processing.[18]

APCVD has some drawbacks compared to conventional CVD such as the high deposition temperature necessary for many chemical reactions and atmosphere condition contaminations. However, using a non-vacuum system has many advantages such as low cost and environment load, easy maintenance and simple configuration.[19]

In addition, APCVD is suitable for large scale deposition and numerous setups are designed and suggested by researchers to meet their needs, making APCVD one of the most flexible deposition methods.

Doping ZnO can significantly increase the conductivity and can be achieved with group III elements such as In,[20] Ga,[21] Al,[22] and B.[23]

Selecting the type of impurity, among other conditions, is very important. The ionic radius of the impurity must be very similar to the ion that is going to substitute for avoiding lattice distortions. The ionic radius of oxygen is very similar to that of fluorine. Also, the coordination number of O and F in ZnO is 4, thus, the substitution should be straightforward. In this situation, fluorine contributes one conduction electron, reducing the resistivity. Among other group III impurities, F does not show as much chemical activities when it enters as a substitute into the ZnO lattice.[24]

EXPERIMENTAL

In this work, we used a homemade chemical vapor deposition apparatus to deposit ZnO films in atmospheric pressure (see Fig. 1).[25]

All the samples were deposited on glass substrates ($75 \times 25 \times 1$ mm^3) by CVD technique in a tube through the oxidation of zinc acetate dihydrate [$C_4H_6O_4Zn{\cdot}2H_2O$, ZnAc] and ammonium fluoride (NH_4F) as a precursor source of fluorine. The initial mass of zinc acetate and NH_4F mixed powder was 0.5 g for all the samples, which was directly

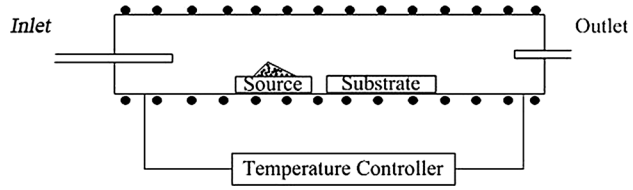

Fig. 1. Air Pressure CVD.

introduced in the reactor. The system contains a horizontal tubular furnace, which has a diameter of 80 mm and length of around 1 m. This furnace is made of quartz to be able to tolerate high temperatures with three heating zones in equal distances from each other with temperature controllers for all heating zones in an attempt to minimize the temperature gradient along the tube.

All the substrates were put in a detergent solution and then rinsed with deionized water. Next, these glass substrates were cleaned with a mixture of deionized water and hydrochloric acid ultrasonically for 20 min. The substrates were again rinsed in deionized water. To prevent undesired oxides on the surface glass substrate while heating, nitrogen flow is used to clean the furnace and substrate before introducing the source materials. This flow was stopped during and after the deposition. This process was chosen based on a few of our experiences between different cleaning processes. The source and substrate are always kept at the same temperature. The distance between the source and substrate is 5 cm. One of the economic advantages of our depositions is the use of air atmosphere as the carrier gas. The deposition duration for each sample was less than 2 min, which is less than some other work with 10 or more minutes of deposition time using the APCVD method,[26,27] depending on the temperature. At lower temperatures, greater time is required to vaporize a fixed amount of 0.5 g as the precursor material. In general, the source material, system geometry, and quantity all affect the local vapor pressure of the reactants present at the substrate and therefore, the properties and morphology of the obtained films.[28]

First, the temperature of zinc acetate was varied from 325°C to 550°C in steps of 25°C to deposit undoped ZnO. By increasing the deposition temperature, the sheet resistance decreased from 17.8 MΩ/□ to 28.9 KΩ/□ as the temperatures varied from 325°C to 450°C. The lowest sheet resistance was obtained at 450°C and was then used as the optimum deposition temperature for the rest of the experiment.

Sheet resistance was further reduced by adding fluorine, in the form of NH_4F, in different weight percentages to the starting powder mix, while the substrate temperature was kept at 450°C as the optimum temperature. The fluorine doping level for the preparation of FZO varied from 2 wt.% to 30 wt.%.

The transmittance spectra were recorded using a UV–Vis spectrophotometer (Perkin-Elmer Lambda 25 UV/vis) in the range of 350–1100 nm. The electrical properties of the thin films were measured by the Hall effect and van der Pauw setup (RH 2010 PhysTech. System). X-ray diffraction was applied to determine the crystalline quality of the samples by using a Cu Kα radiation Philips PW-1800 model. Field emission scanning electron microscopy (FESEM) was carried out by the Mira 3-XMU model for morphological analysis of the thin films. The Swanepoel method[29] was used for thickness measurements of the samples with interference fringes and FESEM cross-section for interference-free thin films.

EDX analysis was implemented, which confirms the chemical composition of fluorine doped ZnO, as can be seen in Fig. 2. Unfortunately, the EDX result could not distinguish the O and F peaks.

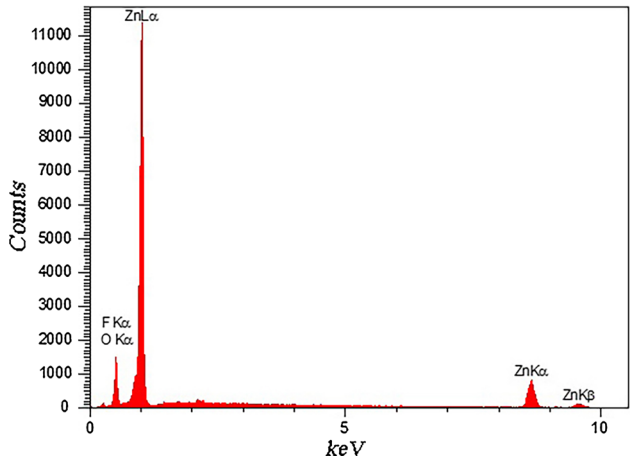

Fig. 2. EDX spectrum measured for fluorine doped ZnO thin films.

RESULTS AND DISCUSSION

Structural Properties

X-ray diffraction patterns for undoped and F doped ZnO thin films are shown in Figs. 3 and 4. The diffraction line related to the (002) plane is the most predominant one at $\theta \approx 34^{\circ}$ which is in agreement with other works.[16] Some other weak peaks corresponding to (100) (101), (103) and (110) are also present. Hence, the crystallites are highly oriented with their *c*-axes, being perpendicular to the substrate surface.[30] The XRD patterns are matched with the hexagonal wurtzite structure of the Joint Committee on Powder Diffraction Standards (JCPDS) reference code 01-075-0576. We could not find any secondary phases corresponding to F, which could be due to the interstitial sites in the ZnO hexagonal lattice structure or the incorporation of F^{-} ions into the oxygen vacancies.[10] As Shinde et al.[31] described, at first, by doping ZnO films, a big hump in the XRD patterns between 20° and 35° is observed. In this stage, not all of the fluorine ions are incorporated into oxygen vacancies yet (2% and 10%), which causes the formation of amorphous plus nanocrystalline phase in the films. Such peak reduction is also reported when moving from undoped to doped samples in another work.[13] By increasing the fluorine concentration (16% and 25%), the number of fluorine ions is such that they could incorporate into most of the oxygen vacancies and therefore, the film structure is almost back to its original (002) structure. Once again, with increasing the dopant percentage (30%), a strong decline is observed as the number of fluorine ions are more than the number of existing oxygen vacancies in the film lattice, therefore, the excess fluorine ions have no specific place in the ZnO lattice, causing the XRD patterns to look like an amorphous structure. This phenomenon is also reported by Noirfalise et al.[32] as a crystalline structure loss in the samples.

Morphological Properties

The surface morphology of the thin films was observed using a field emission scanning electron microscope at room temperature. Figure 5 shows FESEM micrographs of FZO structures deposited on glass substrates with different amounts of fluorine. The distribution, size and microstructure of the FZO thin films change significantly with the fluorine concentration in the CVD source for all the samples.

By increasing the fluorine dopant, at first, we have a surface structure consisting of high density grains with triangle shapes in different sizes (2% doping), and then, the grain shapes change from triangle to a granular surface morphology, which tend to make a bigger cluster (10% doping). By adding more F to the starting powder, we realize more vivid boundaries between the clusters, while the grain sizes in each cluster become smaller (20% doping). Finally, at 30 wt.%, the films exhibit the completely transformed surface morphology of clusters with smooth surfaces and voids between them. The 10% and 20% doped samples show similar morphologies when compared with the 2% and 30% doped samples.

Electrical Properties

While being close to stoichiometry (very low oxygen vacancies in number, which are one of the main electron generation sources), ZnO films show very high sheet resistance, nonstoichiometric ZnO films exhibit much lower sheet resistance. The electrical characteristics of ZnO thin films are mainly dominated by electrons which are generated from Zn interstitial atoms and oxygen vacancies.[33]

Hall effect measurements were executed using the van der Pauw method with a magnetic field of 0.56 T. The samples were cut into square shapes (5×5 mm^2). The silver dots as electrodes were formed at the surfaces corners of each sample.

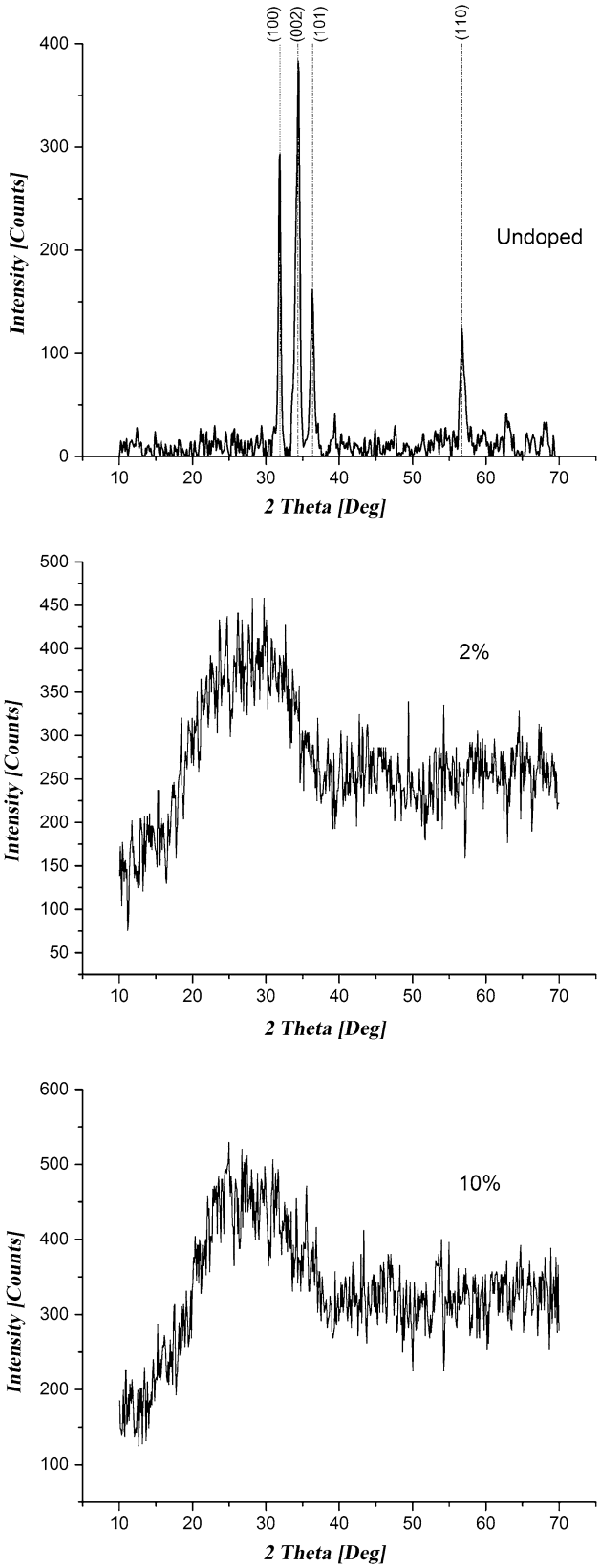

Fig. 3. The XRD pattern of undoped and fluorine doped ZnO thin films deposited with 2% and 10% fluorine concentrations in the CVD source.

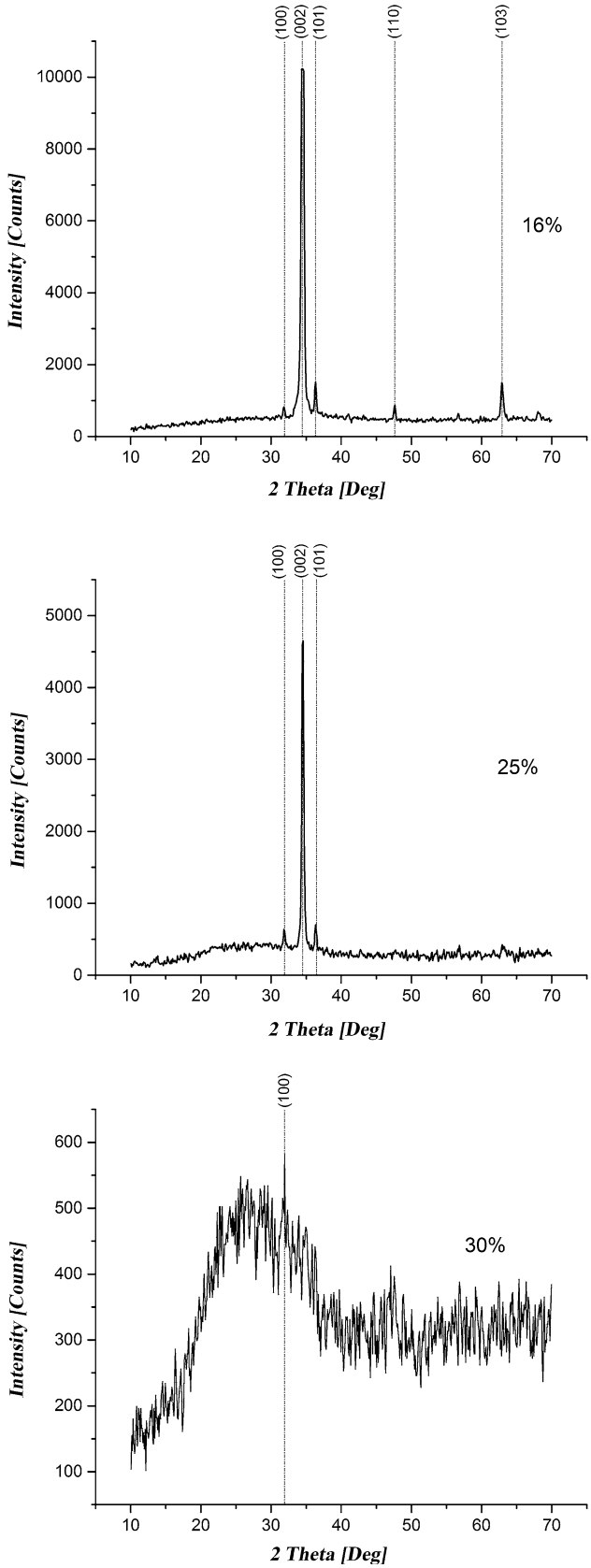

Fig. 4. The XRD pattern of fluorine doped ZnO thin films deposited with 16%, 25%, and 30% fluorine concentrations in the CVD source.

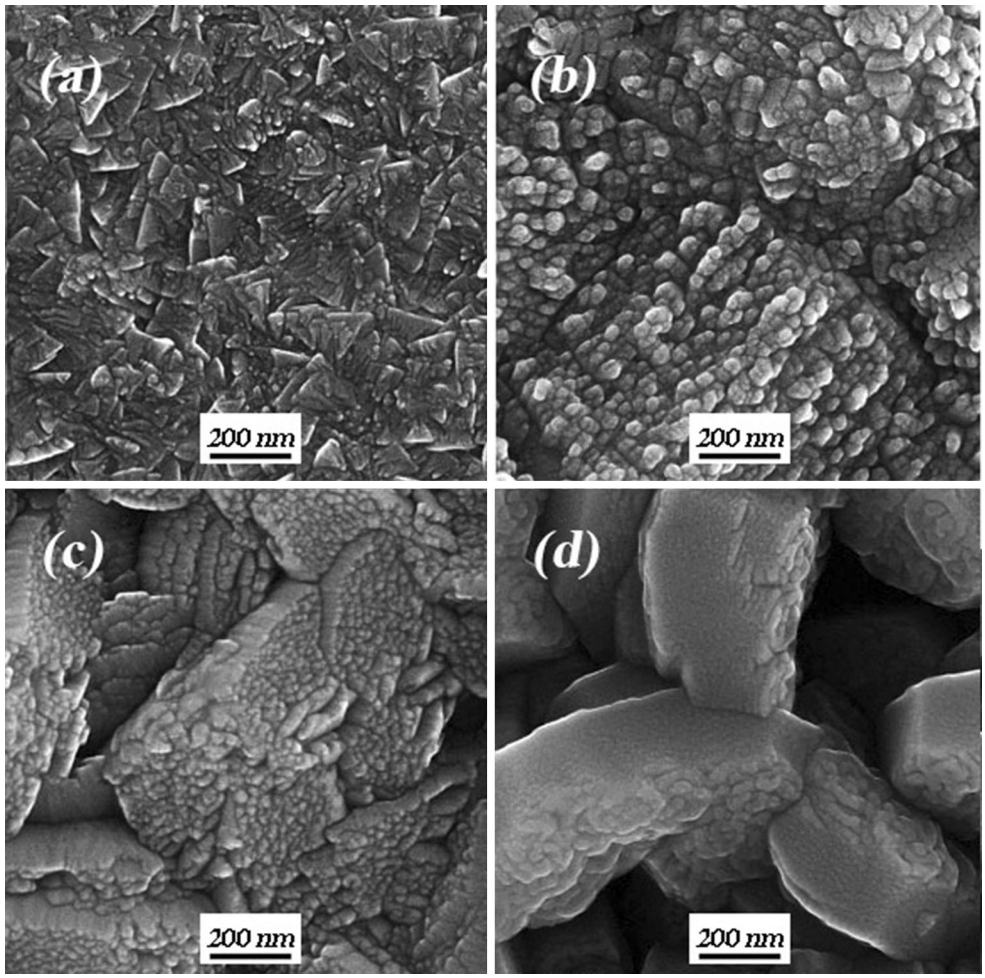

Fig. 5. FESEM images of F doped ZnO films deposited with 2 wt.% (a), 10 wt.% (b), 20 wt.% (c), and 30 wt.% (d) fluorine concentrations in the CVD source.

The variations in the sheet resistance, resistivity, Hall coefficient, mobility and carrier concentration at 450°C are listed in Table I. The lowest sheet resistance was achieved with 20 wt.% of fluorine.

Optical Properties

Figure 6 reveals the optical transmittance spectra in the wavelength range of 300–1100 nm of ZnO thin films as a function of fluorine concentration in the CVD source, which plays an important role in the morphological structure of the films as shown in the "Morphological Properties" section.

The optical constants such as the refractive index, extinction coefficient and absorption coefficient were calculated using the average transmittance in the visible range. The transmittance of the glass substrate only is $T_s = 91.33\%$ in the visible range. Then, the refractive index of the substrate, $s = 1.540754$, is obtained using

$$s = \frac{1}{T_s} + \left(\frac{1}{T_s} - 1\right)^{1/2}. \quad (1)$$

According to the Swanepoel's[29] method which is based on the Manifacier et al.[34] way of making upper and lower envelopes of the transmittance spectrum, the refractive index of the film n in the transparent region, and also, in weak and medium absorption regions, can be calculated using

$$n = \left[N + \left(N^2 - s^2\right)^{1/2}\right]^{1/2}, \quad (2)$$

where

$$N = \frac{2s}{T_m} + \frac{s^2 + 1}{2}$$

for the transparent region and

$$N = 2s\frac{T_M - T_m}{T_M T_m} + \frac{s^2 + 1}{2} \quad (3)$$

for the medium and weak absorption regions. T_m and T_M are the corresponding minimum and maximum transmittance at a certain wavelength, respectively. The thickness of the film is given by:

Table I. Electrical properties of undoped and doped ZnO thin films prepared with different F fluorine concentrations in the CVD source

Doping (wt.%)	Sheet resistance (Ω/□)	Resistivity (Ω cm)	Hall coefficient (cm^3/As)	Mobility (cm^2/Vs)	Carrier concentration (cm^{-3})
0	2.89×10^4	3.98	− 2.54	0.64	2.46×10^{18}
2	64.74	1.01×10^{-2}	− 0.109	10.7	5.68×10^{19}
5	30.70	4.79×10^{-3}	− 0.104	21.8	5.98×10^{19}
10	22.95	3.58×10^{-3}	− 0.145	26.8	4.32×10^{19}
20	17.76	2.77×10^{-3}	-6.11×10^{-2}	21.1	1.02×10^{20}
30	18.91	2.95×10^{-3}	-7.42×10^{-2}	25.2	8.41×10^{19}

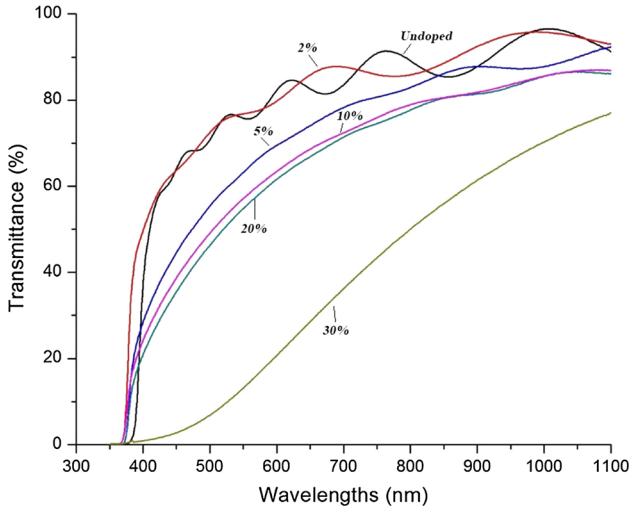

Fig. 6. Optical transmittance spectra for FZO films deposited with different fluorine concentrations in the CVD source.

$$d = \frac{\lambda_1 \lambda_2}{2[\lambda_1 n(\lambda_2) - \lambda_2 n(\lambda_1)]}, \quad (4)$$

where $n(\lambda_1)$ and $n(\lambda_2)$ are the refractive indices at the adjacent minimum (or maximum) at λ_1 and λ_2, respectively. The fundamental equation for interference fringes is $2nd = m\lambda$, where m is an integer for maximum and a half integer for minimum.

The values of thickness were determined using Eq. 4, and for layers with no or not enough interference fringes in the visible region of the transmission spectra; SEM cross-sections were used to measure the layer thickness (Fig. 7). The average thickness for the F doped ZnO films and undoped ZnO layers prepared at 450°C and higher temperatures using SEM cross-sections were around 1600 nm and 1300 nm, respectively.

For these films, the absorption coefficient might be calculated using $\alpha = \left(1/d\right)\ln\left(1/T\right)$,[9,35–37] where d is the film thickness and T is the transmittance of the FZO thin film samples. Since Swanepoel's method is not valid in the strong absorption region, to determine the absorption coefficient of the film in the zone, we used Lambert's formula[38] $\alpha = \left(-1/d\right)\ln T$. The results of the absorption index of the nanostructured FZO thin films as a function of wavelength for different fluorine concentrations in the CVD source are given in Fig. 8.

The optical transitions in semiconductor materials take place by direct and indirect transitions. The dependence of absorption coefficient on photon energy is carried out in the high absorption region to achieve the detailed information about the energy band gaps. The absorption coefficient, α, for direct transitions is expressed by the Tauc's relation[39]

$$\alpha h\nu = B\left(h\nu - E_g\right)^m, \quad (5)$$

where B is an energy-independent constant, α is the material's linear absorption coefficient, E_g is the optical band gap and m is an index that shows the optical absorption process, and it is equal to 2 and ½ theoretically for indirect and direct allowed transitions, respectively. The direct transition across the band gap is attainable between the conduction and valence band edges in k space. In the transition process, the momentum and total energy of the electron-photon system has to be conserved.[40]

In Fig. 9, a straight line is fitted and the extrapolation of this line $E(= h\nu)$ axis indicates the value of the band gap. The plotted graphs belong to the FZO thin films with four different fluorine concentrations in the CVD source. The bandgap values for 5%, 10%, 20%, and 30% of fluorine doping are 3.31 eV, 3.34 eV, 3.37 eV, and 3.33 eV, respectively.

Bandgap energies generally shift by increasing the doping level, and these bandgap blue shifts could be explained according to an increase in carrier concentration which, in turn, can block the conduction band lowest states (also called the Burstein–Moss shift).[41] The BM shift can be written as follows

$$\Delta E_g = \frac{h^2}{8m_e}\left(\frac{3}{\pi}\right)^{2/3} n_e^{2/3}, \quad (6)$$

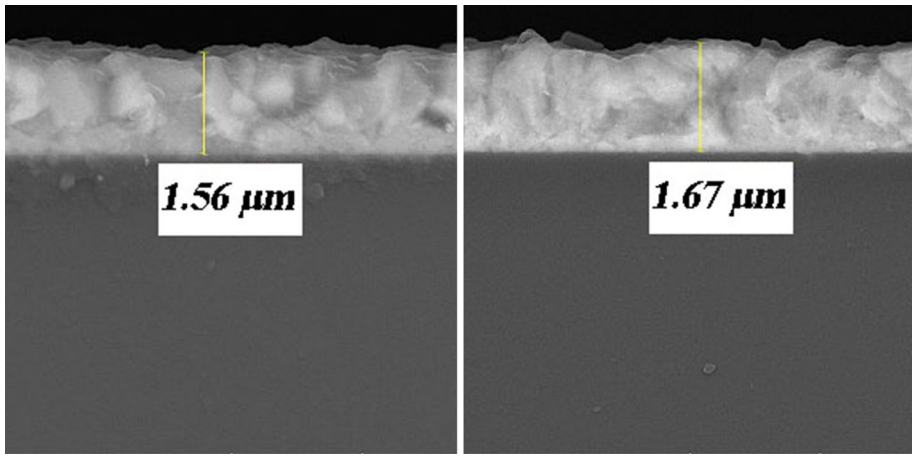

Fig. 7. SEM cross-sections for two of the samples to determine the thickness, 10 wt.% doping (left) and 20 wt.% doping (right).

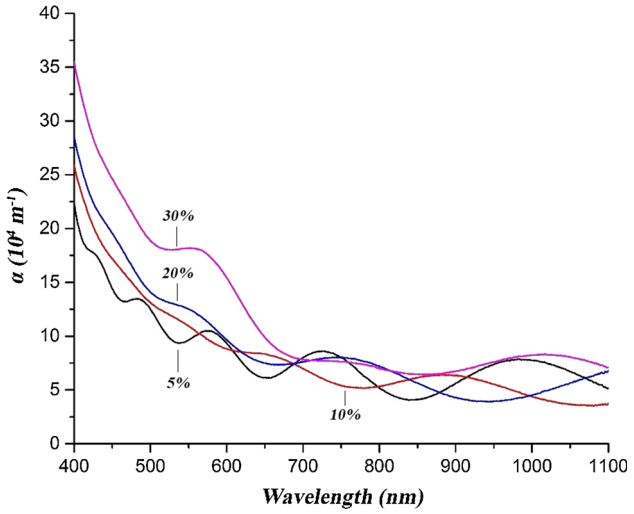

Fig. 8. Variations in absorption coefficient, α, as a function of wavelength for ZnO films with different fluorine concentrations in the CVD source.

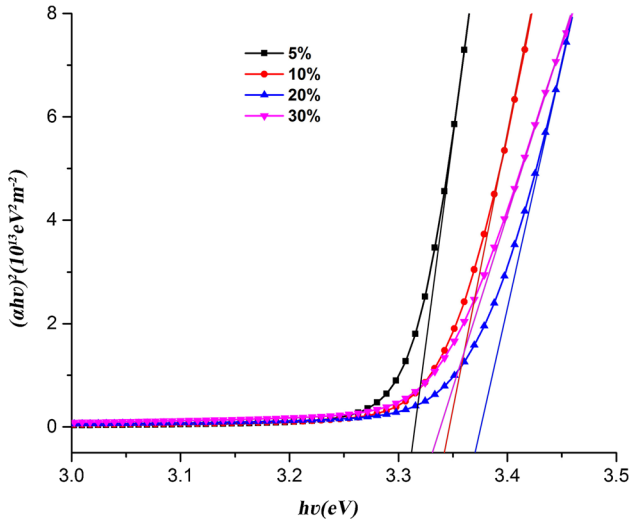

Fig. 9. The dependence of $(\alpha h\nu)^2$ on photon energy E (= $h\nu$) for different fluorine concentrations in the CVD source, from which the optical band gap (E_g) is estimated (Tauc's extrapolation).

where m_e is the effective mass of electrons (≈ 0.28 m_0) in the conduction band and n_e is the carrier concentration. Equation 6 indicates a direct relation between the bandgap shift and carrier concentration.[42]

CONCLUSION

In this work, we presented the synthesis of fluorine doped ZnO nanostructures prepared by atmospheric pressure chemical vapor deposition (APCVD) on glass substrates with different fluorine concentrations in the CVD source in order to achieve the highest optical transparency and electrical conductivity. The XRD patterns of the polycrystalline films showed a hexagonal wurtzite structure with the (002) preferred orientation. Also, the sheet resistance decreased from 28.9 KΩ/□ for the undoped ZnO films to 17.7 Ω/□ for F doped ZnO films using NH_4F as a source of doping.

ACKNOWLEDGEMENTS

The authors gratefully acknowledge the research department of the University of Guilan.

REFERENCES

1. U. Özgür, Y.I. Alivov, C. Liu, A. Teke, M.A. Reshchikov, S. Doğan, V. Avrutin, S.J. Cho, and H. Morkoç, *J. Appl. Phys.* 98, 041301 (2005). https://doi.org/10.1063/1.1992666.
2. J. Yang, X. Liu, L. Yang, Y. Wang, Y. Zhang, J. Lang, M. Gao, and M. Wei, *J. Alloy. Compd.* 485, 743 (2009). https://doi.org/10.1016/j.jallcom.2009.06.070.
3. Z. Li, Z. Hu, L. Jiang, H. Huang, F. Liu, X. Zhang, Y. Wang, P. Yin, and L. Guo, *Appl. Surf. Sci.* 258, 10175 (2012). https://doi.org/10.1016/j.apsusc.2012.06.101.
4. W.W. Liu, B. Yao, Y.F. Li, B.H. Li, Z.Z. Zhang, C.X. Shan, D.X. Zhao, J.Y. Zhang, D.Z. Shen, and X.W. Fan, *Thin*

Solid Films 518, 3923 (2010). https://doi.org/10.1016/j.tsf.2009.12.099.
5. S. Benramache, O. Belahssen, A. Arif, and A. Guettaf, *Opt. Int. J. Light Electron Opt.* 125, 1303 (2014). https://doi.org/10.1016/j.ijleo.2013.08.015.
6. Y.-Z. Tsai, N.-F. Wang, and C.-L. Tsai, *Thin Solid Films* 518, 4955 (2010). https://doi.org/10.1016/j.tsf.2010.03.086.
7. H.S. Yoon, K.S. Lee, T.S. Lee, B. Cheong, D.K. Choi, D.H. Kim, and W.M. Kim, *Sol. Energy Mater. Sol. Cells* 92, 1366 (2008). https://doi.org/10.1016/j.solmat.2008.05.010.
8. A. Maldonado, S. Tirado-Guerra, J.M. Cázares, and M.D.L.L. Olvera, *Thin Solid Films* 518, 2010 (1815). https://doi.org/10.1016/j.tsf.2009.09.039.
9. S. Thonglem, U. Intatha, and S. Eitssayeam, *Ceram. Int.* 41, S331 (2015). https://doi.org/10.1016/j.ceramint.2015.03.215.
10. S. Snega, K. Ravichandran, M. Baneto, and S. Vijayakumar, *J. Mater. Sci. Technol.* 31, 759 (2015). https://doi.org/10.1016/j.jmst.2015.03.001.
11. R. Anandhi, K. Ravichandran, and R. Mohan, *Mater. Sci. Eng. B* 178, 65 (2013). https://doi.org/10.1016/j.mseb.2012.10.001.
12. L. Cao, L. Zhu, J. Jiang, R. Zhao, Z. Ye, and B. Zhao, *Sol. Energy Mater. Sol. Cells* 95, 894 (2011). https://doi.org/10.1016/j.solmat.2010.11.012.
13. T. Minami, S. Ida, T. Miyata, and Y. Minamino, *Thin Solid Films* 445, 268 (2003). https://doi.org/10.1016/s0040-6090(03)01159-3.
14. H. Liang and R.G. Gordon, *J. Mater. Sci.* 42, 6388 (2007). https://doi.org/10.1007/s10853-006-1255-5.
15. J. Hu and R.G. Gordon, *Sol. Cells* 30, 437 (1991). https://doi.org/10.1016/0379-6787(91)90076-2.
16. M. Anusha, D. Arivuoli, E. Manikandan, and M. Jayachandran, *Opt. Mater.* 47, 88 (2015). https://doi.org/10.1016/j.optmat.2015.06.052.
17. M. Anusha and D. Arivuoli, *J. Alloy. Compd.* 580, 131 (2013). https://doi.org/10.1016/j.jallcom.2013.05.073.
18. K.L. Choy, *Prog. Mater Sci.* 48, 57 (2003). https://doi.org/10.1016/S0079-6425(01)00009-3.
19. T. Kawaharamura, *Jpn. J. Appl. Phys.* 53, 05FF08 (2014). https://doi.org/10.7567/jjap.53.05ff08.
20. E.S. Babu and S.K. Hong, *Superlattices Microstruct.* 82, 349 (2015). https://doi.org/10.1016/j.spmi.2015.02.029.
21. H. Jung, D. Kim, and H. Kim, *Appl. Surf. Sci.* 297, 125 (2014). https://doi.org/10.1016/j.apsusc.2014.01.096.
22. E. Arca, K. Fleischer, and I. Shvets, *Thin Solid Films* 555, 9 (2014). https://doi.org/10.1016/j.tsf.2013.08.110.
23. Ü. Alver and A. Tanrıverdi, *Appl. Surf. Sci.* 378, 368 (2016). https://doi.org/10.1016/j.apsusc.2016.04.015.
24. L.M. de la Olvera, A. Maldonado, R. Asomoza, O. Solorza, and D.R. Acosta, *Thin Solid Films* 394, 241 (2001). https://doi.org/10.1016/S0040-6090(01)01164-6.
25. M. Maleki and S.M. Rozati, *Phys. Scr.* 86, 015801 (2012). https://doi.org/10.1088/0031-8949/86/01/015801.
26. M.R. Fadavieslam, H. Azimi-Juybari, and M. Marashi, *J. Mater. Sci. Mater. Electron.* 27, 921 (2015). https://doi.org/10.1007/s10854-015-3835-0.
27. L. Woods and P. Meyers, NREL. p. 1 (2002).
28. A.B. Djurišić, A.M.C. Ng, and X.Y. Chen, *Prog. Quantum Electron.* 34, 191 (2010). https://doi.org/10.1016/j.pquantelec.2010.04.001.
29. R. Swanepoel, *J. Phys. E Sci. Instrum.* 16, 1214 (1983). https://doi.org/10.1088/0022-3735/16/12/023.
30. S. Ilican, M. Caglar, and Y. Caglar, *Mater. Sci. Poland* 25(3), 709 (2007). http://citeseerx.ist.psu.edu/viewdoc/summary?doi=10.1.1.501.2536.
31. S.S. Shinde, P.S. Shinde, S.M. Pawar, A.V. Moholkar, C.H. Bhosale, and K.Y. Rajpure, *Solid State Sci.* 10, 1209 (2008). https://doi.org/10.1016/j.solidstatesciences.2007.11.031.
32. X. Noirfalise, T. Godfroid, G. Guisbiers, and R. Snyders, *Acta Mater.* 59, 7521 (2011). https://doi.org/10.1016/j.actamat.2011.07.068.
33. J.S. Bhat, A.S. Patil, N. Swami, B.G. Mulimani, B.R. Gayathri, N.G. Deshpande, G.H. Kim, M.S. Seo, and Y.P. Lee, *J. Appl. Phys.* 108, 043513 (2010). https://doi.org/10.1063/1.3452333.
34. J.C. Manifacier, J. Gasiot, and J.P. Fillard, *J. Phys. E Sci. Instrum.* 9, 1002 (1976). https://doi.org/10.1088/0022-3735/9/11/032.
35. B. Joseph, P.K. Manoj, and V.K. Vaidyan, *Ceram. Int.* 32, 487 (2006). https://doi.org/10.1016/j.ceramint.2005.03.029.
36. M. Wu, S. Yu, G. Chen, L. He, L. Yang, and W. Zhang, *Appl. Surf. Sci.* 324, 791 (2015). https://doi.org/10.1016/j.apsusc.2014.11.039.
37. D. Hu, X. Liu, S. Deng, Y. Liu, Z. Feng, B. Han, Y. Wang, and Y. Wang, *Physica E* 61, 14 (2014). https://doi.org/10.1016/j.physe.2014.03.007.
38. Y.-J. Choi and H.-H. Park, *J. Mater. Chem. C* 2, 98 (2014). https://doi.org/10.1039/c3tc31478b.
39. J. Tauc, *Amorphous and Liquid Semiconductors* (New York: Springer, 1974). https://doi.org/10.1007/978-1-4615-8705-7.
40. M. Caglar and F. Yakuphanoglu, *Appl. Surf. Sci.* 258, 3039 (2012). https://doi.org/10.1016/j.apsusc.2011.11.033.
41. K. Singh, D.K. Shukla, S. Majid, R. Dhar, R.J. Choudhary, and D.M. Phase, *J. Phys. Conf. Ser.* 755, 012040 (2016). https://doi.org/10.1088/1742-6596/755/1/012040.
42. F.H. Wang, C.F. Yang, and Y.H. Lee, *Nanoscale Res. Lett.* 9, 97 (2014). https://doi.org/10.1186/1556-276X-9-97.